First-principles simulations to understand the structural and electrolyte properties of idealized $Li_{7.5}B_{10}S_{18}X_{1.5}$ (X = Cl, Br, I)

Yan Li ◉ and N. A. W. Holzwarth ◉

Department of Physics, Wake Forest University, Winston-Salem, North Carolina 27109, USA

Recently, researchers at the University of Waterloo (Canada) and Oak Ridge National Laboratory (Oak Ridge, TN) reported a new family of lithium thioborate halide electrolytes with the composition $Li_{7.5}B_{10}S_{18}X_{1.5}$ (X = Cl, Br, I) having very impressive ionic room-temperature conductivity of magnitude $\sigma = 1$ mS/cm. The researchers characterized the structures of the three materials in terms of a well-defined thioborate framework with a void structure containing fractionally occupied Li and X sites. The space group of the materials was identified to be monoclinic ($C2/c$, No. 15). We report the results of first-principles simulations of these materials focusing on understanding the idealized ground-state structures, the mechanisms of Li ion migration, and the overall stability of the materials. A systematic search of many possible stoichiometric crystalline configurations found ordered ground-state realizations of the materials for each of the three halides, X = Cl, Br, I. Molecular dynamics simulations based on the initially ordered structures at various temperatures show significant Li ion hopping within the void channels of the structures at temperatures as low as T = 400 K. Simulations of possible decomposition products suggest that these electrolytes are also chemically stable. Overall, the simulations are consistent with the experimentally reported findings indicating that these materials are very promising solid electrolytes for possible use in solid-state Li ion batteries.

I. INTRODUCTION

The recent work of Kaup *et al.* [1], synthesizing, analyzing, and characterizing lithium thioborate halide electrolytes with the composition $Li_{7.5}B_{10}S_{18}X_{1.5}$ (X = Cl, Br, I), contributes a very encouraging development for all-solid-state battery technology. The authors used the term "superadamantanoid" to describe the cagelike $B_{10}S_{18}$ framework structure. This thioborate framework structure was well characterized by x-ray and neutron diffraction analyses. The three lithium thioborate halide materials have monoclinic space-group symmetry [2] $C2/c$ (No. 15) with highly disordered Li and X sites arranged in the spacious cavities formed within the thioborate framework. The measured room-temperature ionic conductivity having the magnitude of 1 mS/cm puts these electrolytes in the range of superionic conductors such as $Li_{10}GeP_2S_{12}$ [3].

Successful use of boron framework compounds as ionic conductors has been documented in the past literature. For example, the Li boracite $Li_4B_7O_{12}Cl$ [4] has a borate framework that houses a void structure containing Li and Cl ions, but the void volumes are much smaller than those found in the superadamantanoid structure. These lithium boracites are beautiful examples of high-symmetry structures that group theory analysis can predict natural interstitial sites which play important roles in Li ion migration processes. By computationally substituting oxygen in this structure with sulfur to form the thioboracite $Li_4B_7S_{12}Cl$ [5], computation predicts improved Li ion mobility. To our knowledge, $Li_4B_7S_{12}Cl$ has not yet been experimentally realized, and our computations have identified some possible chemical stability issues. On the

other hand, a very recent paper by Kaup *et al.* [6] has shown that it is possible to form $Li_6B_7S_{13}I$ with a very impressive Li ion conductivity. The Cl analog of this material could be obtained, in principle, by adding Li_2S to $Li_4B_7S_{12}Cl$ [7]. Kaup *et al.* [6] also noted that for $Li_6B_7S_{13}I$, the thioborate framework is composed of BS_4 tetrahedra rather than a mix of BS_4 tetrahedra and BS_3 planar triangles found in $Li_4B_7S_{12}Cl$. This Li_6 thioboracite has the same space-group symmetry ($F\bar{4}3c$, No. 219) as members of the Li_4 boracite family at room temperature but has a different occupancy pattern for the Li sites. For $Li_4B_7O_{12}Cl$, analyzed at low temperature according to the $F\bar{4}3c$ space group [8], the Li sites with multiplicity and Wyckoff label $24c$ are fully occupied, while the Li sites $32e$ have a fractional occupancy of $\frac{1}{4}$. By contrast, for $Li_6B_7S_{13}I$, Kaup *et al.* [6] find that the Li sites $24c$ have a fractional occupancy of $\frac{2}{3}$, while the Li sites $32e$ are fully occupied [9]. This change in the Li ion occupancy pattern does result in changes to the Li ion migration mechanisms for the Li_4 and Li_6 boracite families of electrolytes.

Distinct from the high-symmetry boracites and thioboracites which were the focus of previous investigations, the new family of lithium thioborate halide electrolytes presents new challenges. The $Li_{7.5}B_{10}S_{18}X_{1.5}$ materials appear to benefit from low symmetry and large cavity structures housing the Li and halide ions. First-principles simulations on idealized models of these materials can advance our understanding of their structural, stability, and conductivity properties. The remaining sections of the paper are organized as follows. Section II describes the computational methods used in this work. Section III presents the structural optimization results with the

suggested idealized ground-state configurations. Brief results for chemical stability analysis are presented in Sec. IV. First-principles molecular simulations are described and analyzed in Sec. V. The summary and conclusions are presented in Sec. VI.

II. COMPUTATIONAL METHODS

The computational methods used in this work are based on density-functional theory (DFT) [10,11] using the PBEsol [12] exchange-correlation functional and the projector augmented wave (PAW) formalism [13]. The atomic datasets with PAW basis and projector functions were generated by the ATOMPAW code [14]. All simulations were carried out using the QUANTUM ESPRESSO package [15] for the primitive cell of the $C2/c$ structure of four $Li_{7.5}B_{10}S_{18}X_{1.5}$ ($X = $ Cl, Br, I) units (148 atoms). The structural optimization calculations were performed with plane-wave expansions of the wave function including $|\mathbf{k} + \mathbf{G}|^2 \leqslant 81 \, Bohr^{-2}$ and a uniform grid of $2 \times 2 \times 2$ Bloch vectors of $\mathbf{k}$. For the molecular dynamics (MD) simulations, the plane-wave cutoff and Brillouin zone sampling were reduced to $64 \, Bohr^{-2}$ and a single zone-centered $\mathbf{k}$ point, respectively. The first-principles MD simulations were carried out for NVE ensembles (constant number of particles, volume, and total energy), using a time integration step of 2.4 fs. The simulation temperature, as measured from the time-averaged kinetic energy, was controlled by scaling the initial randomized ion velocities. Results of crystal structures and ions mobility were reported in the conventional cell setting of 296 atoms. The VESTA software package [16] was used to construct diagrams of crystal structures. Python [17] and MATLAB [18] codings were employed for calculating and visualizing the ion probability densities using data generated from MD simulations. The symmetry properties of the optimized structures were identified using the FINDSYM program [19].

III. CRYSTAL STRUCTURES

The simplest crystal structures are those whose analyses find all of the symmetry-related atomic positions fully occupied. Luckily, we were able to find such structures as plausible idealized ground states for all of the $Li_{7.5}B_{10}S_{18}X_{1.5}$ materials. Our calculations start from the experimental crystallographic data of $Li_{7.5}B_{10}S_{18}Cl_{1.5}$ obtained from x-ray diffraction measurement of single-crystal samples at room temperature [1]. The reported crystal structure was characterized to have monoclinic space-group $C2/c$ consisting of eight formula units, resulting in 296 atoms per conventional cell. While the B and O sites are fully occupied, the Li and Cl sites are highly disordered. Specifically, the x-ray analysis identified 8 distinct Li sites, which, if fully occupied, would account for 52 of the 60 Li sites per unit cell. Additionally, 3 distinct Cl sites were identified, which, if fully occupied, would represent 16 Cl sites per unit cell, while the stoichiometry allows only 12 Cl sites. The challenge, therefore, was to find 8 additional Li sites and to eliminate 4 Cl sites.

By optimizing a sizable number of symmetry and stoichiometry preserving initial configurations for the missing Cl and additional Li sites on a coarse grid, we found a
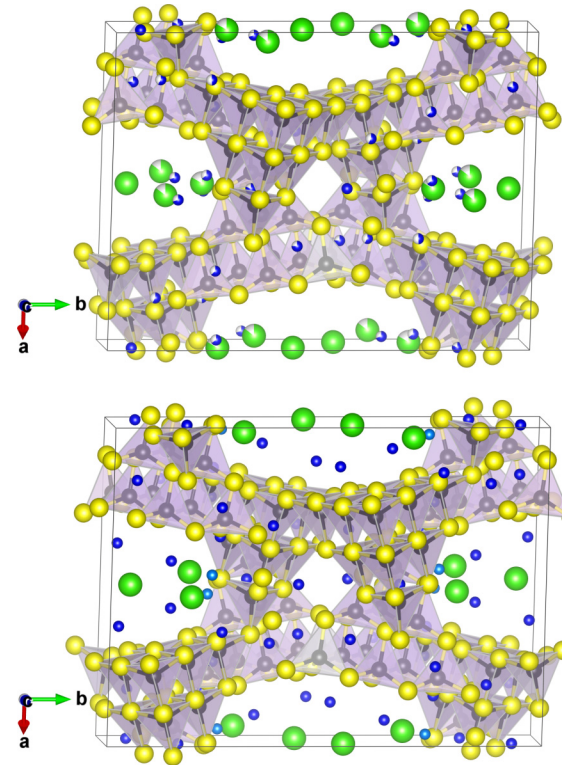

FIG. 1. Structural diagram of a conventional unit cell of $Li_{7.5}B_{10}S_{18}Cl_{1.5}$, visualized along the c axis, comparing (a) the experimental structure deduced from diffraction data of Ref. [1] with (b) the optimized structure of this work. The Li, B, S, and Cl ions are represented by blue, black, yellow, and green balls, respectively, and the BS_4 tetrahedra are also indicated. In the experimental diagram (a), the fractional occupancy is indicated with the fractionally filling of the colored balls. In the optimized structural diagram (b), the Li(9) sites are indicated by light blue balls.

likely candidate for the idealized ground-state structure of $Li_{7.5}B_{10}S_{18}Cl_{1.5}$. The ideal structure was calculated to have an energy of more than 0.1 eV per conventional cell lower than the energies of the other candidate structures. The optimized lattice parameters are compared with the experiment in Table I. The missing Cl sites were the $4e$ Wyckoff sites labeled Cl(1) by Kaup *et al.* [1]. The additional Li sites were found as $8f$ sites labeled Li(9). The distinct optimized fractional coordinates for Li and Cl in $Li_{7.5}B_{10}S_{18}Cl_{1.5}$ are compared with corresponding x-ray single-crystal values in Table II and the experimental and idealized structures are illustrated in Fig. 1(b).

Comparing the polyhedral drawings shown in Fig. 1 for the experimental and optimized crystal structures, we find that the placements of the B-S framework in the two crystals are remarkably similar. To some extent, our ideal model has position profiles of Li and Cl ions similar to those of experimental measurements, except that the Li ions are more dispersed and uniformly distributed in the ordered representative structure. The placement of the additional Li(9) type Li ions is indicated in Fig. 1(b) with light blue balls. Interestingly, Table II shows good agreement between the computed and the experimentally analyzed fractional positions of the distinct Li and Cl sites, apart from the missing Cl(1) and added Li(9).

TABLE I. Summary of lattice parameters for the most stable ordered phases of $Li_{7.5}B_{10}S_{18}X_{1.5}$ with X = Cl, Br, I. The experimental results are from Kaup *et al.* [1], Table 1.

	X = Cl (cal./exp.)	X = Br (cal./exp.)	X = I (cal./exp.)
a (Å)	20.96/21.14	20.88/21.17	21.09/21.28
b (Å)	21.66/21.20	21.19/21.45	21.40/21.42
c (Å)	16.02/16.22	16.07/16.11	16.08/16.15
$\alpha = \gamma$ (deg)	90.00/90.00	90.00/90.00	90.00/90.00
β (deg)	128.75/128.92	128.43/128.68	128.70/128.72

The largest differences are less than 0.2 fractional units, and these occur for Li(4) and Li(5) which are located in the void cavities. MD simulations find these sites to be among the most active in Li ion migration as will be discussed in Sec. V.

Since the three crystalline halides $Li_{7.5}B_{10}S_{18}X_{1.5}$ (X = Cl, Br, I) have the same space-group symmetry with similar lattice parameters and atomic positions, it is reasonable to construct the initial configurations for the rest of the halide materials simply by substituting Br or I ions for Cl ions in the idealized $Li_{7.5}B_{10}S_{18}Cl_{1.5}$ structure instead of using the corresponding reported crystallographic data with diverse fractional occupancy on the Li and X sites.

To summarize the optimization results, we list in Table I the optimized lattice parameters and monoclinic angles. There is generally good agreement between experiment and theory and also quite a few similarities between the three halide materials. In more detail, we see from Table I that some of the optimized lattice parameters differ from the experimental values by as much as 0.5 Å. In fact, there is a variation of up to 0.2 Å comparing Table 1 and Table S1 in the experimental paper of Ref. [1], perhaps due to different measurement and sample preparation methods. It seems quite likely that lattice strain due to the Li and halide disorder in the experimental samples can cause size variations relative to the idealized crystals and also among various sample preparations. Interestingly, both experiment and computation find the lattice parameters for the three materials to be remarkably similar even though the ionic radii of the three halides differ substantially. Presumably

this result follows from the fact that the halide ions are well accommodated within the cavity regions in all three materials.

Listed in Table II are the fractional coordinates of the inequivalent Li and X atoms determined from the optimization studies. For $Li_{7.5}B_{10}S_{18}Cl_{1.5}$ the Li and Cl coordinates are compared with the experimental values for Li(1)–Li(8) and Cl(2)–Cl(3). Interestingly, the fractional coordinates for each distinct Li and halide site are quite similar for the three materials. For completeness, the fractional coordinates of B and S framework ions are listed for the Cl halide in the Appendix Table VI, showing good agreement with the corresponding experimental values. Fractional coordinates for the framework ions of the other halide materials are very similar and also show good agreement with experiment.

The optimized ordered structural models for all three different halides, together with the drawings of experimental structures, are shown in Fig. 2. In order to improve the clarity of the visualization, we represent the B-S bonds in the framework with thin sticks so that we can easily see the Li and halide positions. It is not out of our expectation to find the general likeness between these diagrams, although there are indeed some differences, for example, in the arrangement patterns of Li and X ions.

The experimental report [1] also includes analysis of the neutron scattering in terms of the pair distribution function $G(r)$, which we have reproduced in Fig. 3(a). To examine our idealized structures, the radial pair distribution function can also be simulated from our MD trajectories $\{\mathbf{R}_i(t)\}$ for all ions

TABLE II. Summary of inequivalent fractional positions (x, y, z) of Li and X ions for the most stable ordered phases of $Li_{7.5}B_{10}S_{18}X_{1.5}$ with X = Cl, Br, I. The experimental results are from Kaup *et al.* [1], Table S2. The column "Wyck" lists the the multiplicity and Wyckoff label for the $C2/c$ space group in the conventional cell setting.

| Atom	Wyck	X = Cl (cal.)/(exp.)	X = Br (cal.)	X = I (cal.)
Li(1)	$4e$	(0.000, 0.170, 0.250)/(0.000, 0.165, 0.250)	(0.000, 0.166, 0.250)	(0.000, 0.167, 0.250)
Li(2)	$4e$	(0.500, 0.437, 0.250)/(0.500, 0.437, 0.250)	(0.500, 0.433, 0.250)	(0.500, 0.434, 0.250)
Li(3)	$8f$	(0.166, 0.946, 0.953)/(0.174, 0.943, 0.962)	(0.172, 0.945, 0.956)	(0.169, 0.945, 0.955)
Li(4)	$8f$	(0.427, 0.143, 0.224)/(0.471 0.240, 0.373)	(0.407, 0.101, 0.241)	(0.397, 0.092, 0.223)
Li(5)	$8f$	(0.875, 0.521, 0.087)/(0.971, 0.341, 0.074)	(0.896, 0.547, 0.048)	(0.589, 0.538, 0.032)
Li(6)	$8f$	(0.314, 0.374, 0.283)/(0.342, 0.384, 0.284)	(0.327, 0.376, 0.292)	(0.325, 0.374, 0.289)
Li(7)	$4d$	(0.250, 0.250, 0.500)/(0.250, 0.250, 0.500)	(0.250, 0.250, 0.500)	(0.250, 0.250, 0.500)
Li(8)	$8f$	(0.357, 0.259, 0.055)/(0.348, 0.269, 0.084)	(0.367, 0.247, 0.057)	(0.359, 0.252, 0.055)
Li(9)	$8f$	(0.036, 0.267, 0.562)/(no exp. data ——)	(0.048, 0.281, 0.547)	(0.055, 0.283, 0.548)
X(1)	$4e$	(no calc. values —)/(0.500, 0.233, 0.250)		
X(2)	$8f$	(0.035, 0.311, 0.883)/(0.030, 0.359, 0.975)	(0.028, 0.341, 0.904)	(0.028, 0.345, 0.903)
X(3)	$4e$	(0.000, 0.550, 0.250)/(0.000, 0.554, 0.250)	(0.000, 0.518, 0.250)	(0.000, 0.497, 0.250)
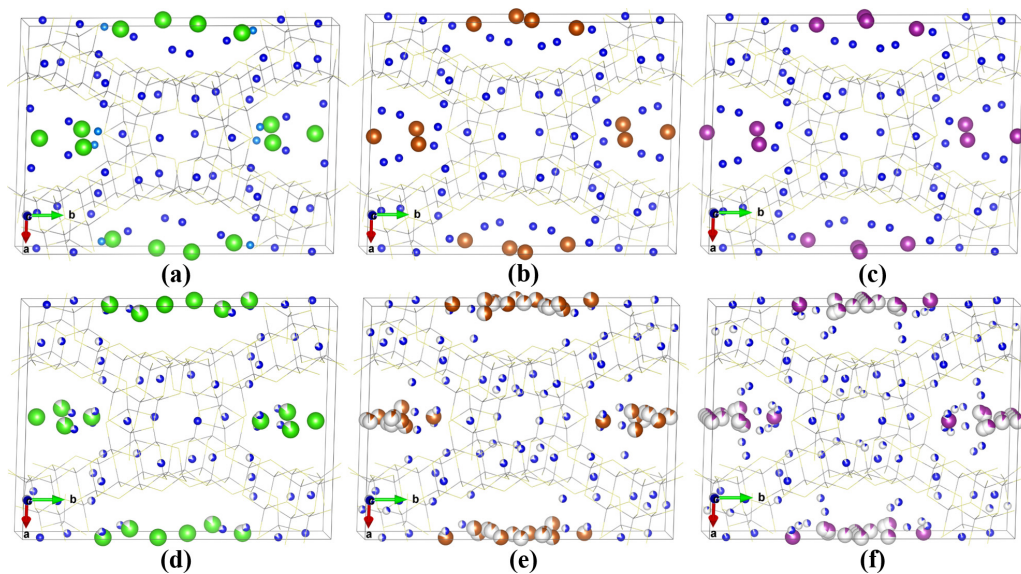
FIG. 2. Visualization of structural results for the three different halides $Li_{7.5}B_{10}S_{18}X_{1.5}$ with X = Cl (a and d), Br (b and e), I (c and f), comparing computationally optimized structures on the top row with the structures deduced by Kaup *et al.* [1] on the bottom row. The color representations are the same as in Fig. 1 except that the B-S bonds in the framework structure are represented by thin sticks. Cl, Br, and I ions are represented green, brown, and purple balls, repsectively. Fractional occupancy of sites in the experimental analysis is represented by partially filled spheres.

i in the simulation according to the expression [20], [21].

$$G(r) = \frac{1}{4\pi r^2 N \rho} \left\langle \sum_{i=1}^{N} \sum_{j \neq i}^{N} \delta(r - |\mathbf{R}_i(t) - \mathbf{R}_j(t)|) \right\rangle_t. \quad (1)$$

Here N is the number of ions in the simulation cell which has a number density of ρ. $\mathbf{R}_i(t)$ denotes the simulated position of ion i at time t. In practice, the summation over j excludes $j = i$ within the simulation cell but includes equivalent ions in periodic images of the simulation cell. The angular brackets in the expression represent the averaging over time steps t over

FIG. 3. Plots of the pair distribution functions for $Li_{7.5}B_{10}S_{18}X_{1.5}$ with X = Cl (red), Br (blue), I (green) comparing results from analysis of (a) the experimental neutron diffraction measurements by Kaup *et al.* [1] and (b) Eq. (1) using trajectories $\mathbf{R}_i(t)$ from MD simulations at $\langle T \rangle \approx 400$ K, averaged over 30 ps of simulation time.

30 ps of MD simulations. In practice, the δ function in Eq. (1) was evaluated with a one-dimensional Gaussian function with a root mean-squared width of 0.1 Å.

Figure 3(b) shows that the simulation peak profiles match both qualitatively and quantitatively the values of $G(r)$ determined from neutron-scattering results on powdered samples reported in Ref. [1] shown in Fig. 3(a). Interestingly, the profiles of calculated pair distribution with respect to the spatial distance are remarkably similar for the three materials $Li_{7.5}B_{10}S_{18}X_{1.5}$ with X = Cl, Br, I. This was also noted by Kaup *et al.* [1] and follows from the fact that $G(r)$ is dominated by contributions from the $B_{10}S_{18}$ framework ions. Nevertheless, the agreement between experiment and simulation results for $G(r)$ provides additional assurance that these idealized ground-state structures of $Li_{7.5}B_{10}S_{18}X_{1.5}$ are consistent with the experimental findings.

IV. STABILITY ANALYSIS

To address the question of chemical stability of the lithium thioborate halide compounds, we investigated several decomposition reactions for $Li_{7.5}B_{10}S_{18}X_{1.5}$ for each of the halides, X = Cl, Br, I as listed in the first column of Table III. The reaction energies are estimated from the ground-state static lattice energies (from DFT) for each material involved in the reactions, neglecting the vibrational energy contributions and other more sophisticated considerations. Within this approximation, the reaction energies, estimated by subtracting the sum of energies of the products from the energy of the reactant, are found to be positive in all of the cases considered as listed in Table III. Although the present computational investigation is not the whole story, it does provide reasonable evidence of the expected chemical stability of the three halide materials.
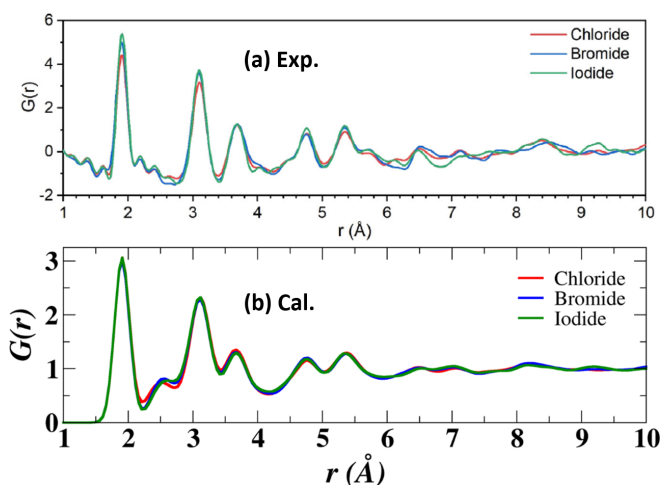
TABLE III. Computed energy differences ($\Delta U_{SL} = U_{SL}^P - U_{SL}^R$) between reactants (R) and products (P) for reactions indicated by the first column. All energies are given in eV units.

Reaction: $R \rightarrow P$	$\Delta U_{SL}(X = \text{Cl})$	$\Delta U_{SL}(X = \text{Br})$	$\Delta U_{SL}(X = \text{I})$
$\text{Li}_{7.5}\text{B}_{10}\text{S}_{18}X_{1.5} \rightarrow 1.5\,\text{Li}X^{\text{a}} + 6\,\text{Li}^{\text{b}} + 10\,\text{B}^{\text{c}} + 18\,\text{S}^{\text{d}}$	25.54	25.60	25.68
$\text{Li}_{7.5}\text{B}_{10}\text{S}_{18}X_{1.5} \rightarrow 1.5\,\text{Li}X^{\text{a}} + 6\,\text{Li}^{\text{b}} + 5\,\text{B}_2\text{S}_3^{\text{e}} + 3\,\text{S}^{\text{d}}$	13.12	13.17	13.25
$\text{Li}_{7.5}\text{B}_{10}\text{S}_{18}X_{1.5} \rightarrow 1.5\,\text{Li}X^{\text{a}} + 2\,\text{Li}_3\text{BS}_3^{\text{f}} + 4\,\text{B}_2\text{S}_3^{\text{e}}$	0.99	1.05	1.13
$\text{Li}_{7.5}\text{B}_{10}\text{S}_{18}X_{1.5} \rightarrow 1.5\,\text{Li}X^{\text{a}} + 3\,\text{Li}_2\text{S}^{\text{g}} + 5\,\text{B}_2\text{S}_3^{\text{e}}$	0.83	0.89	0.97

[a]Cubic with space-group $Fm\bar{3}m$ (No. 225).
[b]Cubic with space-group $Im\bar{3}m$ (No. 229).
[c]Rhombohedral with space-group $R\bar{3}m$ (No. 166); from Ref. [22].
[d]Orthorhombic with space-group $Fddd$ (No. 70); from Ref. [23].
[e]Tetragonal with space-group $I4_1/a$ (No. 88); from Ref. [24].
[f]Orthorhombic with space-group $Pnma$ (No. 62); from Ref. [25].
[g]Cubic with space-group $Fm\bar{3}m$ (No. 225).

V. ANALYSIS OF MD SIMULATIONS

MD simulations performed at a given average temperature $\langle T \rangle$ provide insight into the mechanism of ionic transport in the lithium thioborate halides in terms of the trajectories $\mathbf{R}_i^u(t)$ of each ion i of type u at time t. We are particularly interested in the motions of the Li and halide ions. In this work, we adapted the ideas of He $et\ al.$ [20] to determine a probability density in the form

$$p_u(\mathbf{r}) = \frac{1}{k_{\max}} \sum_{k=1}^{k_{\max}} \sum_{i \in u} \delta\big(\mathbf{r} - \mathbf{R}_i^u(t_k)\big). \quad (2)$$

Here $\mathbf{r}$ denotes a lattice position that a u type ion visits, t_k is the sampling time, and $k_{\max}$ represents the number of time steps considered in the analysis. By definition, the integral of $p_u(\mathbf{r})$ throughout the crystal cell is the total number of u type ions N^u. In practice, the evaluation is based on the MD trajectories represented in the conventional simulation cell. The delta function in the definition is approximated by an isotropic three-dimensional Gaussian shape

$$\delta(\mathbf{s}) \approx \frac{1}{(2\pi\sigma^2)^{3/2}} e^{-s^2/2\sigma^2} \quad (3)$$

with σ chosen as 0.2 Å. Equation (2) for $p_u(\mathbf{r})$ approximates the probability density as the time fraction per unit volume that an ion of type u spends at position $\mathbf{r}$.

Figure 4 shows the colored isosurfaces of constant probability values superposed on the optimized structural diagrams, plotting separately for Li ions in the top row and $X = $ Cl, Br, I ions in the bottom row. As expected, the isosurfaces encompass the equilibrium positions of the Li and halide ions in the ground-state structures. It is evident that there are remarkably similar shapes between the three halides.

For the Li probability densities, we note that by rotating the visualization to other directions, we found that most Li ions contribute to ionic current as they are observed to move extensively within the crystal along three-dimensional migration pathways. These pathways are both within the cavity space and also thread through the thioborate framework. More information we can perceive is that the relatively easy conduction of Li ions in each material is attributed to the low barrier energy between neighboring sites. It is reasonable to speculate

that the disorder within the Li ion sublattice in these systems is a critical determinant to the superior Li conducting behavior.

By contrast, the motions of halogens X ($X = $ Cl, Br, I) are confined within the void channels of each of the crystals, presenting distribution patterns actually compatible with those disordered arrangements of X ions of the experimental structures shown in Fig. 1.

Focusing on the motions of the Li ions, it is possible to further analyze the MD trajectories to obtain information about the specific Li ion sites that participate in Li ion transport. The specific Li ions sites are referenced by spheres of radius 1 Å centered about each equilibrium Li ion position. Our scheme works by tracking the motions of each migrating Li ion at each time step and monitoring the occupancy or vacancy of each of the reference spheres. As noted in Table II, there are 9 distinct Li sites and 60 total Li sites in each conventional unit cell [26]. For each time step of the MD trajectories, each of the Li ions could be identified with a unique label corresponding to an instance of an equilibrium positions of type Li(1)–Li(9) or 0, on the basis of its position within one or none of the reference spheres, respectively. In addition to the position label at each time step, the actual distance to the equilibrium site location was also recorded. With this information, the occupation patterns of the equilibrium spheres could be analyzed. In particular, for each Li ion of the simulation cell, its "arrival" time at a given reference sphere was recorded as the time step where its distance to the labeled equilibrium position was the shortest. In this way, the trajectory of each Li ion of the simulation was parameterized as a list of arrival times and their corresponding reference sites, which could be used for further analysis. For example, it is used to obtain information about the specific Li ion sites involved with Li ion transport. Here the arrival time lists were used to accumulate the occupation times of different unique sites for each material and produce the histogram plot as shown in Fig. 5. To be specific, the number of visitors of a given site type counts the number of times that a mobile Li ion hops into any of its equivalent sites from a nearest-neighbor site during the full 50-ps simulation. In this sense, the comparisons of Fig. 5 indicate that the Li(4) and Li(5) type sites, located within the large void cavities, are most highly visited sites.

For comparison, a related measure of Li ion migration is the vacancy formation energy which can be determined by
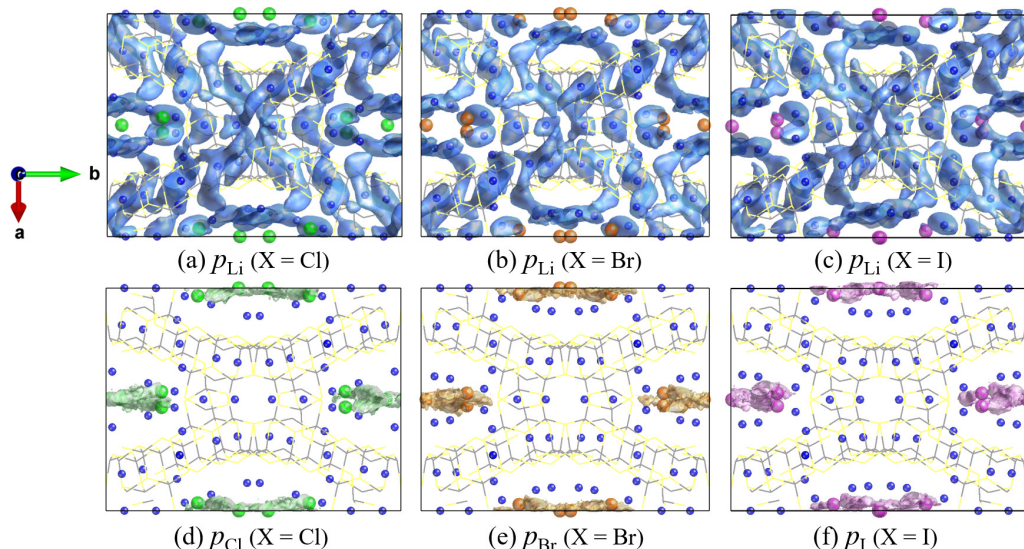
(a) p_{Li} (X = Cl)   (b) p_{Li} (X = Br)   (c) p_{Li} (X = I)

(d) p_{Cl} (X = Cl)   (e) p_{Br} (X = Br)   (f) p_I (X = I)

FIG. 4. Isosurface plots of $p_u(\mathbf{r}) = 0.04$ Å^{-3} for Li (a, b, and c) and X (d, e, and f) ions in Li$_{7.5}$B$_{10}$S$_{18}$X$_{1.5}$ with X = Cl, Br, I visualized along the c axis. The results are determined from MD simulations at $\langle T \rangle$ = 768, 775, and 779 K, respectively. The B$_{10}$S$_{18}$ units are represented by the thin sticks.

relaxing the ideal lattice structure with one missing Li ion from a unique host position in the presence of a uniform compensation charge of the opposite sign. The computed relative total electronic energies are summarized in Table IV.

It is encouraging to note that those most popular (most visited) sites are exactly the ones—Li(4), Li(5), and Li(8)—with the lowest vacancy energies, listed in Table IV. On the one hand, the agreement corroborates our proposed scheme for analyzing Li ion hopping events; on the other hand, it implies that the most probable conduction path of Li ions is formed by the energetically favorable sites with approximately similar energies. Such phenomenon observed for Li$_{7.5}$B$_{10}$S$_{18}$X$_{1.5}$ (X = Cl, Br, I) is compatible with the common features of fast ionic conductors.
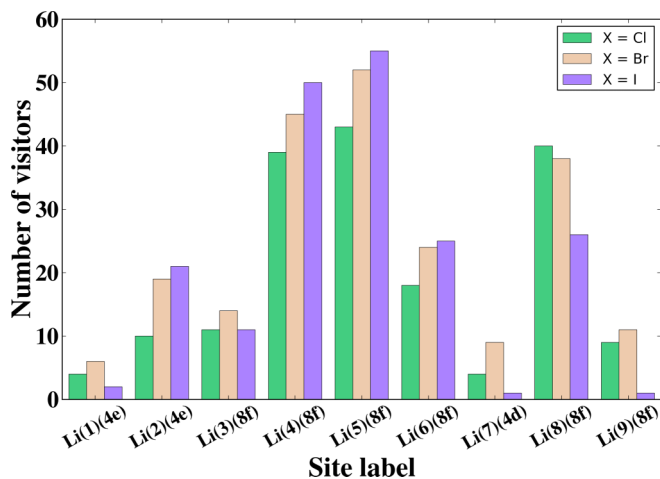

FIG. 5. Histograms of the number of visitors of each host site type with label indicated on the horizontal axes for Li$_{7.5}$B$_{10}$S$_{18}$X$_{1.5}$ with X = Cl (green), Br (brown), and I (violet). The values of vertical axes are obtained from MD simulations of 50 ps duration using primitive cell models at $\langle T \rangle$ = 768, 775, and 779 K, respectively.

In principle, a more quantitative picture of Li ion diffusion properties is provided by its mean-squared displacement (MSD) as a function of time interval τ and average simulation temperature T,

$$\mathrm{MSD}(\tau, T) = \frac{1}{N^{Li}} \left\langle \sum_{i=1}^{N^{Li}} \left| \mathbf{R}_i^{Li}(t + \tau) - \mathbf{R}_i^{Li}(t) \right|^2 \right\rangle_t. \quad (4)$$

In this expression, only the Li ion trajectories are included, and the angular brackets denote averaging over Li configurations at each time step t. N^{Li} denotes the number of mobile Li ions in the simulation cell.

Figure 6 shows the MSD results for Li$_{7.5}$B$_{10}$S$_{18}$Cl$_{1.5}$ averaged over time intervals of up to 70 ps for five different average temperatures from 400 to 800 K. It is impressive to observe that there is appreciable Li ion migration at a temperature as low as 400 K. As the temperature increases, the diffusion coefficient increases as Li ions gain more thermal energy to overcome the migration barriers to move a greater distance.

TABLE IV. Vacancy energies E_v (in eV/formula unit) for unique vacancy sites in Li$_{7.5}$B$_{10}$S$_{18}$X$_{1.5}$ (X = Cl, Br, I). The zero of energy was taken to be the lowest vacancy energy for each material.

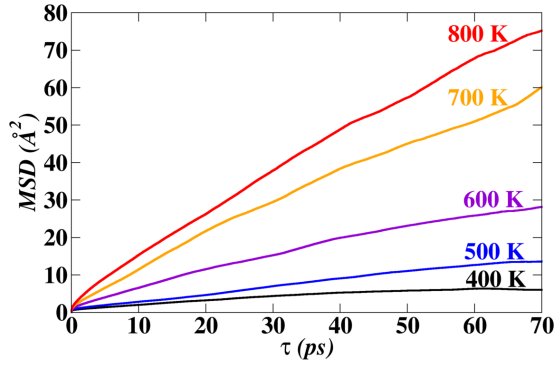| Site	Wyck	E_v (X = Cl)	E_v (X = Br)	E_v (X = I)
Li(1)	$4e$	0.167	0.148	0.136
Li(2)	$4e$	0.141	0.096	0.101
Li(3)	$8f$	0.177	0.138	0.128
Li(4)	$8f$	0.000	0.000	0.010
Li(5)	$8f$	0.000	0.000	0.010
Li(6)	$8f$	0.176	0.145	0.133
Li(7)	$4d$	0.212	0.176	0.160
Li(8)	$8f$	0.000	0.003	0.000
Li(9)	$8f$	0.075	0.143	0.130

FIG. 6. MSD plot for Li ions of $Li_{7.5}B_{10}S_{18}Cl_{1.5}$ at various simulation temperatures as indicated by the text near each curve.

MSD(τ, T) is related to the tracer diffusion $D_{tr}(T)$ which is defined as

$$D_{tr}(T) = \lim_{\tau \to \infty}\left(\frac{1}{6\tau}\, MSD(\tau, T)\right). \qquad (5)$$

The dependence of the tracer diffusion coefficient on temperature follows an Arrhenius behavior

$$D_{tr}(T) = D_{ref}\, e^{-E_a/k_B T}, \qquad (6)$$

where k_B is Boltzmann constant, and the prefactor D_{ref} and activation energy E_a are deduced from fitting the natural log of the calculated $D_{tr}(T)$ values to a linear function of $1/T$. From the diffusion coefficients evaluated at various temperatures, we can approximate the conductivity of Li ions based on the Nernst-Einstein relationship

$$\sigma(T) = \frac{N^{Li}}{V}\frac{e^2 D_{tr}(T)}{k_B T H_r}, \qquad (7)$$

where V is the volume of the simulation cell, e is the elemental charge for Li ions, and H_r is the Haven ratio which represents correlations between different Li ions relative to the tracer diffusion contribution [20,27,28]. This analysis assumes that the halide ions do not contribute to the ionic conductivity. Given the results for the halide probability isosurfaces shown in Fig. 4, indicating that the halide motions are largely confined within the void regions, this seems like a reasonable approximation.

Figure 7 presents the Li ion conductivities for the iodide, bromide, and chloride materials, estimated from the MD results, compared with the experimental measurements reported by Kaup and co-workers [1]. The general trend of the computational results is that the iodide material displays the best ionic conductivity performance followed by the bromide and the chloride materials. This qualitative feature is consistent with the experimental results superposed on this diagram and as evidenced by the quantitative results of activation energies listed in Table V.

Nevertheless, it is not possible to ignore the fact that the comparison of ionic conductivity between the experiment and the calculation shows a significant numerical discrepancy. The measured room-temperature ionic conductivities for the three halides are found to be about 1 mS/cm, while the simulated results are overestimated by more than a factor of 10. There are many possible reasons for the quantitative discrepancy
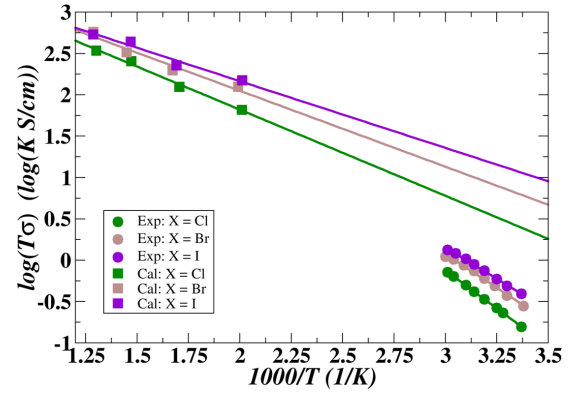

FIG. 7. Plots of Li ion conductivity from MD simulations using Eq. 7 with $H_r = 1$ in comparison with experimental conductivity measurements.

between simulations and experiment. For example, the MD simulations use idealized crystals at constant volume and elevated temperatures while experiments are performed on powdered samples at room temperature. Another possible contribution to this discrepancy between the theory and the experiment can be ascribed to the simplistic approximation for the Haven ratio. The simulation results assumed $H_r = 1$, which corresponds to the notion of uncorrelated Li ion motions in the transport process. This approach has been used by many authors and works quite well to identify fast ion conductors, for example, as shown by He *et al.* [29]. However, it is often the case that the Li ion hopping events are not independent as observed for other classes of superionic conductors [20].

While Haven [27] experimentally investigated the relationship between D_{tr} and ionic conductivity by measuring both on the same samples with the help of radio active isotopes, theoretical/computational estimates are difficult. For simple crystals, the correlation effects can be estimated from geometric considerations [28]. More generally, quantitative estimates of ionic correlations in MD simulations are very difficult due to large statistical fluctuations in the terms involving correlations of pairs of different ions. The corresponding terms involving self-correlations have much more manageable statistical fluctuations, as used in the evaluation of the tracer diffusion $D_{tr}(T)$ of Eq. (5). Several authors such as He *et al.* [20] have computed the Haven ratio for particular ionic materials, despite the difficulty. A very recent paper [30] develops a "spectral denoising approach" which seems very promising for computing these ionic correlations.

In the present study, the MD trajectories are examined for qualitative evidence of correlated Li ion motion. We note

TABLE V. Arrhenius activation energies E_a for $Li_{7.5}B_{10}S_{18}X_{1.5}$ (X = Cl, Br, I), comparing experimental results from Ref. [1] with the calculated values derived from the slopes of the fitted lines in Fig. 7.

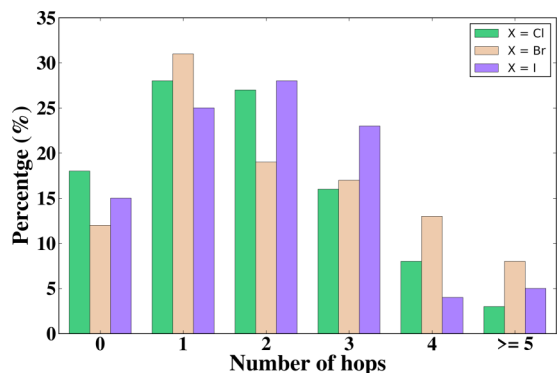| Halides	Exp (eV)	Cal (eV)
Cl	0.36	0.21
Br	0.33	0.18
I	0.30	0.16

FIG. 8. Frequency distribution of number of hopping events of Li ions in time interval of 0.5 ps for $Li_{7.5}B_{10}S_{18}X_{1.5}$ with X = Cl (green), Br (brown), and I (violet). The values of vertical axes are obtained from MD simulations of 50 ps duration using primitive cell models at $\langle T \rangle$ = 768, 775, and 779 K, respectively.

that the determined ground-state structures of $Li_{7.5}B_{10}S_{18}X_{1.5}$ are fully ordered; however, it is highly likely that at least some of Li ions reside in very shallow equilibria. Therefore the migration mechanism may be more complicated than a simple motion of a host Li ion moving to an interstitial site. For example, perhaps there is a continuum of interstitial sites available to the migrating Li ions which can be analyzed from a MD trajectory, using spheres of radius 1 Å about each equilibrium Li site as reference, as mentioned in the site occupancy analysis above.

In order to obtain information about time correlations in the Li ion motion, the parameterized trajectory data were analyzed in terms of hopping events. For each Li ion, the difference between two consecutive arrival times gives a reasonable measure of the time for a hopping event to occur. Inspired by ideas presented by He *et al.* [20], the accumulated list of hopping times can now be analyzed as a histogram to determine how many hopping events occur within various time intervals. In this work, we chose to base the histogram analysis on the time interval of $\Delta t = 0.5$ ps using MD trajectories at average temperature $\langle T \rangle \approx 800$ K for the three ideal models of $Li_{7.5}B_{10}S_{18}X_{1.5}$ (X = Cl, Br, I). In order to construct the histograms for each material and each of the Li ion trajectories, we examined 100 time intervals Δt in terms of the number of hopping events that occurred. The resulting histograms of numbers of Li ion hops is presented in Fig. 8, with different bar colors representing the three different materials. The figure shows that for each material, the percentage of time intervals experiencing 0 or 1 hops is less than 50%. This means that the intervals experiencing 2 or more hops account for more than 50%. Therefore, this analysis provides strong evidence that the mechanisms for Li ion diffusion in $Li_{7.5}B_{10}S_{18}X_{1.5}$ (X = Cl, Br, I) are likely to involve multi-ion concerted migration processes.

VI. CONCLUSIONS

Using first-principles modeling techniques, we found plausible representative ordered models for the three lithium thioborate halide materials $Li_{7.5}B_{10}S_{18}X_{1.5}$ (X = Cl, Br, I) recently discovered by Kaup *et al.* [1]. The rationality of the

theoretical models is evidenced by the remarkable similarity of structural profile with the experimental report. From the knowledge of the idealized optimized structures, the group of materials is evaluated to be chemically stable against decomposing into possible decomposition products, as detailed in Table III. In terms of electrolyte properties, the results of MD simulations show remarkable three-dimensional Li ion mobility within the void regions and through the $B_{10}S_{18}$ framework at temperatures as low as 400 K and higher, agreeing with the experimental findings. By contrast, the halide ions are found to be confined within the void cavities. By proposing a reasonable hopping model based on MD trajectories, we are able to identify a concerted mechanism for the Li ion motions primarily within the void cavities. Both simulation and experiment suggest that the iodide material shows the highest ionic conductivity, followed by bromide and chloride. However, the MD simulation results greatly overestimated the ionic conductivity with an order of magnitude different from 1 mS/cm of the experimental measurement at room temperature. There are several possible reasons for this discrepancy, including estimating the conductivity solely based on the MSD analysis for Li ions, which does a poor job of modeling concerted Li ion motions and neglects effects due to halide motion. Our trajectory analysis summarized in Fig. 8

TABLE VI. Fractional coordinates of unique $B_{10}S_{18}$ framework ions in $Li_{7.5}B_{10}S_{18}Cl_{1.5}$ comparing near room-temperature x-ray data reported by Kaup *et al.* in Ref. [1] with the computed results. Each unique B ion and S ion occupies sites with multiplicity and Wyckoff label $8f$.

Atom	Exp (x, y, z)	Calc (x, y, z)
B1	(0.044, 0.159, 0.466)	(0.047, 0.161, 0.469)
B2	(0.089, 0.131, 0.017)	(0.084, 0.132, 0.013)
B3	(0.091, 0.069, 0.194)	(0.086, 0.071, 0.190)
B4	(0.123, 0.214, 0.202)	(0.119, 0.214, 0.200)
B5	(0.226, 0.103, 0.011)	(0.221, 0.103, 0.003)
B6	(0.229, 0.042, 0.183)	(0.225, 0.044, 0.179)
B7	(0.262, 0.185, 0.190)	(0.259, 0.184, 0.188)
B8	(0.266, 0.123, 0.368)	(0.263, 0.125, 0.366)
B9	(0.267, 0.484, 0.143)	(0.274, 0.487, 0.149)
B10	(0.294, 0.263, 0.369)	(0.290, 0.260, 0.367)
S1	(0.011, 0.231, 0.128)	(0.007, 0.233, 0.120)
S2	(0.021, 0.085, 0.384)	(0.026, 0.089, 0.385)
S3	(0.022, 0.151, 0.565)	(0.028, 0.151, 0.570)
S4	(0.113, 0.054, 0.096)	(0.108, 0.056, 0.091)
S5	(0.147, 0.204, 0.105)	(0.144, 0.203, 0.103)
S6	(0.151, 0.139, 0.288)	(0.147, 0.140, 0.285)
S7	(0.159, 0.163, 0.544)	(0.163, 0.166, 0.549)
S8	(0.181, 0.283, 0.293)	(0.177, 0.281, 0.292)
S9	(0.239, 0.404, 0.073)	(0.239, 0.409, 0.075)
S10	(0.241, 0.468, 0.235)	(0.242, 0.473, 0.236)
S11	(0.256, 0.027, 0.093)	(0.250, 0.030 0.086)
S12	(0.288, 0.175, 0.099)	(0.284, 0.174, 0.093)
S13	(0.295, 0.111, 0.277)	(0.292, 0.111, 0.274)
S14	(0.294, 0.052, 0.455)	(0.285, 0.054, 0.450)
S15	(0.323, 0.255, 0.278)	(0.320, 0.253, 0.276)
S16	(0.326, 0.191, 0.461)	(0.327, 0.190, 0.460)
S17	(0.383, 0.496, 0.223)	(0.390, 0.500, 0.227)
S18	(0.389, 0.379, 0.079)	(0.393, 0.375, 0.085)

suggests that correlated motion may play an important role in these materials. Additionally, grain boundary effects may also play a role in reducing the ideal conductivity of experimental samples, as suggested by Kaup *et al.* [6] in comparing computed and measured ionic conductivity for $Li_6B_7S_{13}Cl$. More careful study should also include lattice expansion effects that may also be important for these materials. However, we expect that the computation results presented in this work do provide insight into the fundamental and technical properties of $Li_{7.5}B_{10}S_{18}X_{1.5}$ ($X = Cl$, Br, I) for their promising application as electrolytes in all-solid-state batteries.

APPENDIX: STRUCTURAL DETAILS

While the experimental structural analysis of the three $Li_{7.5}B_{10}S_{18}X_{1.5}$ compounds had significant uncertainty in the Li and X ion positions, Kaup *et al.* [1] found the positions of the $B_{10}S_{18}$ framework ions to be well defined and similar. The calculated fractional coordinates of the framework ions are in very good agreement with the near room-temperature x-ray diffraction analysis as shown in Table VI for $Li_{7.5}B_{10}S_{18}Cl_{1.5}$. Similar agreement is seen for the other two crystals.

[1] K. Kaup, A. Assoud, J. Liu, and L. F. Nazar, Angew. Chem., Int. Ed. **60**, 6975 (2021).

[2] M. I. Aroyo, J. M. Perez-Mato, D. Orobengoa, E. Tasci, G. De La Flor, and A. Kirov, Bulgarian Chem. Commun. **43**, 183 (2011); M. I. Aroyo, J. M. Perez-Mato, C. Capillas, E. Kroumova, S. Ivantchev, G. Madariaga, A. Kirov, and H. Wondratschek, Z. Krist. **221**, 15 (2006); M. I. Aroyo, A. Kirov, C. Capillas, J. M. Perez-Mato, and H. Wondratschek, Acta Cryst. A**62**, 115 (2006). Available at the website https://www.cryst.ehu.es/

[3] N. Kamaya, K. Homma, Y. Yamakawa, M. Hirayama, R. Kanno, M. Yonemura, T. Kamiyama, Y. Kato, S. Hama, K. Kawamoto, and A. Mitsui, Nat. Mater. **10**, 682 (2011).

[4] Yan Li and N. A. W. Holzwarth, Phys. Rev. Materials **6**, 025401 (2022).

[5] Y. Li, First Principles Investigations of Electrolyte Materials in All-Solid-State Batteries, Ph.D. thesis, Wake Forest University (2021), available from the website https://wakespace.lib.wfu.edu/handle/10339/99397/. An additional publication related to the Li boracite family of materials is being prepared in collaboration with D. Cory Lynch.

[6] K. Kaup, K. Bishop, A. Assoud, J. Liu, and L. F. Nazar, J. Am. Chem. Soc. **143**, 6952 (2021).

[7] Kaup *et al.* [6] also noted that for $Li_6B_7S_{13}I$, the thioborate framework is composed BS_4 tetrahedra rather than a mix of BS_4 tetrahedra and BS_3 planar triangles found in $Li_4B_7S_{12}Cl$.

[8] W. Jeitschko, T. A. Bither, and P. E. Bierstedt, Acta Crystallogr., Sect. B: Struct. Sci., Cryst. Eng. Mater. **33**, 2767 (1977), detailed crystal parameters associated with this work are available as cif files from various crystallography databases.

[9] Note that by shifting the fractional coordinates reported by Kaup *et al.* [6] by $(\frac{1}{4}, \frac{1}{4}, \frac{1}{4})$, the symmetry analysis of $Li_6B_7S_{13}X$ can be compared more directly with the analysis of γ-$Li_4B_7O_{12}Cl$ originally reported by Jeitschko *et al.* [8].

[10] P. Hohenberg and W. Kohn, Phys. Rev. **136**, B864 (1964).

[11] W. Kohn and L. J. Sham, Phys. Rev. **140**, A1133 (1965).

[12] J. P. Perdew, A. Ruzsinszky, G. I. Csonka, O. A. Vydrov, G. E. Scuseria, L. A. Constantin, X. Zhou, and K. Burke, Phys. Rev. Lett. **100**, 136406 (2008).

[13] P. E. Blöchl, Phys. Rev. B **50**, 17953 (1994).

[14] N. A. W. Holzwarth, A. R. Tackett, and G. E. Matthews, Comput. Phys. Commun. **135**, 329 (2001), available from the website http://pwpaw.wfu.edu.

[15] P. Giannozzi, O. Baseggio, P. Bonfà, D. Brunato, R. Car, I. Carnimeo, C. Cavazzoni, S. de Gironcoli, P. Delugas, F. Ferrari Ruffino, A. Ferretti, N. Marzari, I. Timrov, A. Urru, and S. Baroni, J. Chem. Phys. **152**, 154105 (2020), available from the website quantumespresso.org.

[16] K. Momma and F. Izumi, J. Appl. Crystallogr. **44**, 1272 (2011).

[17] Python Software Foundation. Python Language Reference, version 3.8. Available at https://www.python.org.

[18] MATLAB, 2021, version 9.10.0.1602886 (R2021a), The MathWorks Inc., Natick, MA, 2010. Available at https://www.mathworks.com.

[19] H. T. Stokes and D. M. Hatch, J. Appl. Crystallogr. **38**, 237 (2005), available from the webpage https://stokes.byu.edu/iso/findsym.php.

[20] X. He, Y. Zhu, and Y. Mo, Nat. Commun. **8**, 15893 (2017).

[21] The expression used in Ref. 20 is more general than Eq. (1), considering trajectories of ions i and j, $\mathbf{R}_i(t)$ and $\mathbf{R}_j(t + \Delta t)$, at different time steps, which is not needed for the pair distribution function.

[22] B. Morosin, A. W. Mullendore, D. Emin, and G. A. Slack, AIP Conf. Proc. **140**, 70 (1986).

[23] S. J. Rettig and J. Trotter, Acta Crystallogr. Sect. C **43**, 2260 (1987).

[24] T. Sasaki, H. Takizawa, K. Uheda, T. Yamashita, and T. Endo, J. Solid State Chem. **166**, 164 (2002).

[25] P. Vinatier, P. Gravereau, M. Ménétrier, L. Trut, and A. Levasseur, Acta Crystallographica Section C **50**, 1180 (1994).

[26] In practice, simulations were carried out in the primitive unit cell but results are reported for the conventional unit cell.

[27] Y. Haven and B. Verkerk, Phys. Chem. Glasses **6**, 38 (1965).

[28] G. E. Murch, Solid State Ionics **7**, 177 (1982).

[29] X. He, Q. Bai, Y. Liu, A. M. Nolan, C. Ling, and Y. Mo, Adv. Energy Mater. **9**, 1902078 (2019).

[30] N. Molinari, Y. Xie, I. Leifer, A. Marcolongo, M. Kornbluth, and B. Kozinsky, Phys. Rev. Lett. **127**, 025901 (2021).